

Nonlinear fluid damping of elastically mounted pitching wings in quiescent water

Yuanhang Zhu ^{1†}, Varghese Mathai ² and Kenneth Breuer ¹

¹Center for Fluid Mechanics, School of Engineering, Brown University, Providence, RI 02912, USA

²Department of Physics, University of Massachusetts, Amherst, MA 01003, USA

(Received xx; revised xx; accepted xx)

We experimentally study the nonlinear fluid damping of a rigid but elastically mounted pitching wing in the absence of a freestream flow. The dynamics of the elastic mount are simulated using a cyber-physical system. We perturb the wing and measure the fluid damping coefficient from damped oscillations over a large range of pitching frequencies, pitching amplitudes, pivot locations and sweep angles. A universal fluid damping scaling is proposed to incorporate all these parameters. Flow fields obtained using particle image velocimetry are analyzed to explain the nonlinear behaviors of the fluid damping.

1. Introduction

The interaction between elastically mounted pitching wings and unsteady flows is central to many applications. With a free-stream flow, this interaction can lead to self-sustained, flow-induced oscillations, which have been studied for understanding classic aeroelastic behaviour (Dowell *et al.* 1989; Dugundji 2008), as well as in developing oscillating foil energy harvesting devices (Xiao & Zhu 2014; Young *et al.* 2014). Without a free stream, but with prescribed heaving or flapping (i.e. hovering), the passive flow-induced pitching motions are used in modelling the thrust generation and maneuvering in animal flight (Wang 2005; Bergou *et al.* 2007; Shinde & Arakeri 2013; Kang & Shyy 2014; Beatus & Cohen 2015).

One of the critical parameters that govern the flow-structure interactions of passively pitching wings is the fluid damping. According to the semi-empirical Morison equation (Morison *et al.* 1950), the total fluid force exerted on a wing submerged in unsteady viscous fluid can be divided into two parts – the force associated with fluid inertia (i.e. the added mass force), which is in phase with acceleration (Brennen 1982; Corkery *et al.* 2019), and the force induced by vortices in the flow (i.e. the fluid damping force), which is in phase with velocity (Shih & Buchanan 1971; Kang & Shyy 2014; Su & Breuer 2019). While the structural damping force is typically proportional to velocity because of the constant structural damping coefficient, the fluid damping force is expected to scale quadratically with velocity (Morison *et al.* 1950; Keulegan & Carpenter 1958), and due to this nonlinearity, the fluid damping coefficient is usually obtained empirically as a function of the reduced frequency, the Reynolds number, the oscillation amplitude, etc (Shih & Buchanan 1971). For pitching flexible wings (Alben 2008) and heaving membrane wings (Tzezana & Breuer 2019), the fluid damping coefficient is found to scale inversely with the oscillation frequency.

† Email address for correspondence: yuanhang_zhu@brown.edu

For elastically mounted pitching wings with a free stream, the interplay between the fluid damping and the structural damping governs the flow-induced oscillation. By mapping out the cycle-averaged energy transfer between the elastic system and the ambient fluid using prescribed kinematics, Menon & Mittal (2019) and Zhu *et al.* (2020) showed that the energy injected by the negative fluid damping must be equal to the energy dissipated by the positive structural damping in order for the flow-induced oscillations to sustain. In other words, the total damping of the system must be zero (Dugundji 2008). The negative fluid damping arises primarily from the formation and shedding of dynamic stall vortices (McCroskey 1982; Corke & Thomas 2015). In the absence of a free stream, however, the fluid damping becomes positive and counteracts the pitching motion because of the drag effect. With both the fluid damping and the structural damping being positive, any perturbations to the system will be damped out. However, little is known about how the fluid damping shapes the damped oscillations, and understanding this is of critical importance for understanding the fluid-structure interactions of elastically mounted pitching wings under external perturbations such as gusts.

In the present study, we use laboratory experiments to characterise the fluid damping of elastically mounted pitching wings in quiescent water, with the elastic mount simulated using a cyber-physical system (§2). We perform ‘ring down’ experiments to extract the fluid damping (§3.1). The effects of many parameters are investigated, including the effects of the pitching frequency, the pitching amplitude, the pivot location and the sweep angle (§3.2). We propose a universal fluid damping scaling to incorporate these parameters (§3.3), and correlate the nonlinear behaviour of the fluid damping with the dynamics of the vortical structures measured using particle image velocimetry (§3.4). Finally, the key findings are summarised in §4.

2. Experimental set-up

Figure 1(a) shows a schematic of the experimental set-up. We conduct all the experiments in the Brown University free-surface water tunnel (test section width \times depth \times length = 0.8 m \times 0.6 m \times 4.0 m), with the flow speed kept at zero ($U_\infty = 0$ m/s). A NACA 0012 wing, made of clear acrylic, is mounted vertically in the tunnel, with an endplate on the top to skim surface waves and eliminate wingtip vortices at the root. The wing is connected to a six-axis force/torque transducer (ATI 9105-TIF-Delta-IP65), which measures the fluid torque τ_f exerted on the wing. This τ_f is then fed into the cyber-physical system (CPS). Depending on the input virtual structural parameters, specifically the torsional stiffness k_v , damping b_v and inertia I_v , the CPS calculates the pitching position of the wing and outputs the signal to the servo motor (Parker SM233AE). An optical encoder (US Digital E3-2500) which is independent of the CPS is used to measure the pitching position θ . The CPS is operated at 4000 Hz to minimise any phase delay between the input τ_f and the output θ . A detailed explanation of the CPS can be found in Zhu *et al.* (2020).

We use two-dimensional particle image velocimetry (PIV) to measure the flow field around the wing. The flow is seeded using 50 μ m diameter hollow ceramic spheres and illuminated by a laser sheet at the mid-span plane. The laser sheet is generated by a double-pulse Nd:YAG laser (532 nm, Quantel EverGreen) with LaVision sheet optics. The transparent wing enables flow field measurements on both sides of the wing. Due to the limitation of space beneath the tunnel, a 45° mirror is used to reflect the images into two co-planar sCMOS cameras (LaVision). We use the DaVis software (LaVision) to calculate (two passes at 64 \times 64 pixels, two passes at 32 \times 32 pixels, both with 50% overlap) and stitch the velocity fields from the two cameras to form a field of view of 3.2c \times 3.2c, where c is the chord length of the wing.

Figure 1(b) sketches the two types of wings we use in the present study. For the unswept

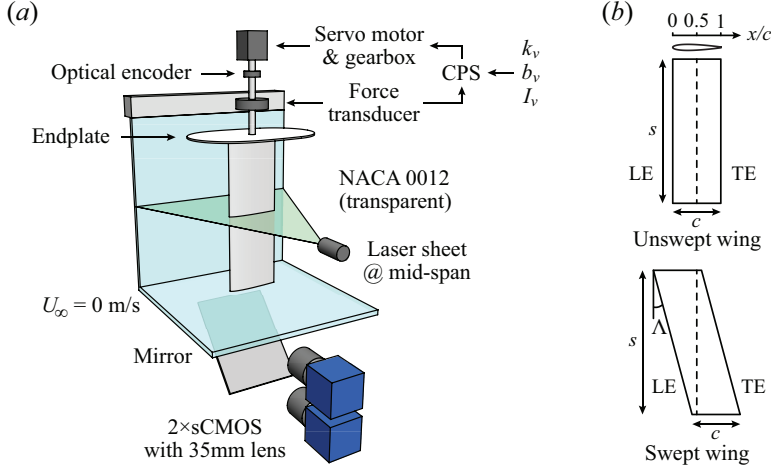


FIGURE 1. (a) A schematic of the experimental set-up. The structural dynamics of the wing is simulated by a cyber-physical system (CPS). (b) Sketches of unswept and swept wings. The leading edge (LE) and the trailing edge (TE) are parallel. Dashed lines represent the pivot axis.

wing, a wing holder mechanism (not shown) enables the pivot axis to be adjusted between $x/c = 0$ and 1 with a step size of 0.125. For the swept wings, the sweep angle Λ is defined as the angle between the leading edge and the vertical axis. Four swept wings with $\Lambda = 10^\circ$, 15° , 20° and 25° are used. As shown in the figure, the pivot axis of swept wings is a vertical line passing through the mid-chord point ($x/c = 0.5$) of the mid-span plane. All the wings have a span of $s = 0.3$ m and a chord length of $c = 0.1$ m, which results in an aspect ratio of $AR = 3$.

The governing equation of the system is

$$I\ddot{\theta} + b\dot{\theta} + k\theta = \tau_f, \quad (2.1)$$

where θ , $\dot{\theta}$, and $\ddot{\theta}$ are the angular position, velocity and acceleration, respectively. I , b and k are the effective inertia, damping and stiffness of the system. The effective inertia I is the sum of the virtual inertia I_v , which we prescribe with the CPS, and the physical inertia I_p of the wing (i.e. $I = I_v + I_p$). The effective damping b equals the virtual damping b_v (i.e. $b = b_v$) because the friction in the system is negligible. The effective stiffness k equals the virtual stiffness (i.e. $k = k_v$). τ_f is the nonlinear fluid torque experienced by the wing, which can be divided into the added mass torque, $\tau_a = -I_a\ddot{\theta}$, where I_a is the added fluid inertia, and the fluid damping torque, for simplicity $\tau_b = -b_f\dot{\theta}$, where b_f is the fluid damping coefficient (see §1). Note that b_f is expected to be a function of $\dot{\theta}$ (Mathai *et al.* 2019). Equation 2.1 can thus be rearranged as

$$(I + I_a)\ddot{\theta} + (b + b_f)\dot{\theta} + k\theta = 0. \quad (2.2)$$

After a perturbation of amplitude A_0 is applied at time t_0 , the damped oscillations of the system can be described as

$$\theta = A_0 e^{-\gamma(t-t_0)} \cos [2\pi f_p(t-t_0)], \quad (2.3)$$

where

$$\gamma = \frac{b + b_f}{2(I + I_a)} \quad \text{and} \quad f_p = \frac{1}{2\pi} \sqrt{\frac{k}{I + I_a} - \gamma^2}. \quad (2.4a, b)$$

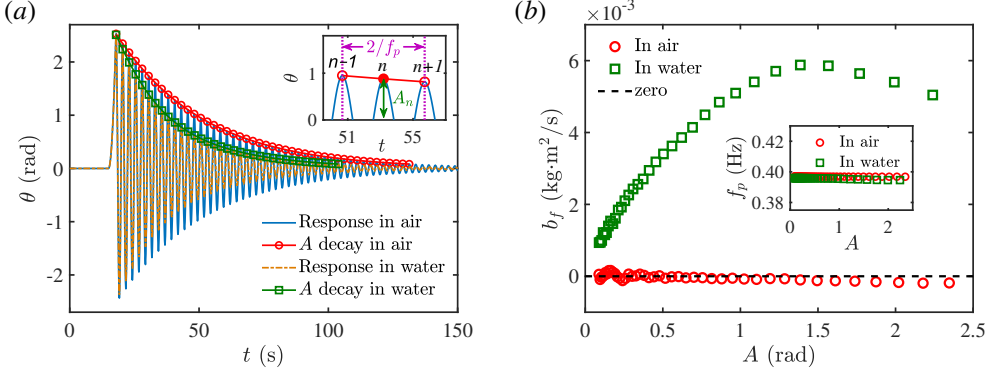


FIGURE 2. (a) System response and amplitude decay in a typical ‘ring down’ test, where an elastically mounted unswept wing ($\Lambda = 0^\circ$) pivots around the mid-chord ($x/c = 0.5$) at a frequency of $f_p = 0.40$ Hz. The inset shows the measurements of the pitching amplitude A_n and the pitching frequency f_p of the n -th peak. The fluid damping b_f at A_n is extracted by fitting an exponential curve (i.e. the red solid line) to the adjacent three peaks. (b) Extracted b_f in air and in water. The zero value is indicated by the black dashed line. The inset compares the measured pitching frequency f_p in air and in water.

3. Results and Discussion

3.1. Extracting the fluid damping from ‘ring down’ experiments

We conduct ‘ring down’ experiments to measure the fluid damping experienced by elastically mounted pitching wings. In the ‘ring down’ experiment, a short-time constant-torque impulse is applied to the CPS as the perturbation, after which the system response and the amplitude decay of the wing is recorded and analysed. Figure 2(a) shows the results from a typical ‘ring down’ experiment. In this specific case, we use an unswept wing ($\Lambda = 0^\circ$) which pivots around the mid-chord ($x/c = 0.5$) at a frequency of $f_p = 0.40$ Hz. We conduct the ‘ring down’ experiment twice – once in air and once in water. The pitching amplitude of the wing decays faster in water than in air, indicating a higher total damping in water.

To quantify this amplitude decay, the positive peaks of the system response are identified. As shown in the inset, the amplitude of the n -th peak is denoted by A_n , and the corresponding pitching frequency is measured as $f_p = 2/(t_{n+1} - t_{n-1})$. To measure the total damping $b + b_f$ at amplitude A_n , we fit an exponential, $y = \alpha e^{-\gamma t}$, to the three adjacent peaks, $n - 1$, n and $n + 1$, and extract the corresponding γ (see equation 2.3). Now the only unknown in equation 2.4b is the added mass, I_a . After obtaining I_a , the fluid damping, b_f , is then calculated using equation 2.4a (Rao 1995). Since f_p and γ are both measured, I_a and b_f are also *measured* quantities. Moreover, both I_a and b_f are *cycle-averaged*, meaning they cannot reflect the instantaneous variation of the fluid inertia and damping. The measured fluid damping, b_f , in both air and water are compared in figure 2(b). Since τ_f in equation 2.1 is negligible in air as compared to other forces in the equation, b_f stays near zero, which is indicated by the good agreement between the red circles and the black dashed line. As shown by the green squares, b_f in water is significant because of the existence of the fluid damping torque, τ_b . It is also observed that b_f in water increases non-monotonically with A . This nonlinear behaviour will be revisited later in §3.4. The inset of figure 2(b) shows the measured pitching frequency, f_p , in both air and water. Due to the combined effect of the fluid inertia and damping, we see that f_p is slightly lower in water than in air.

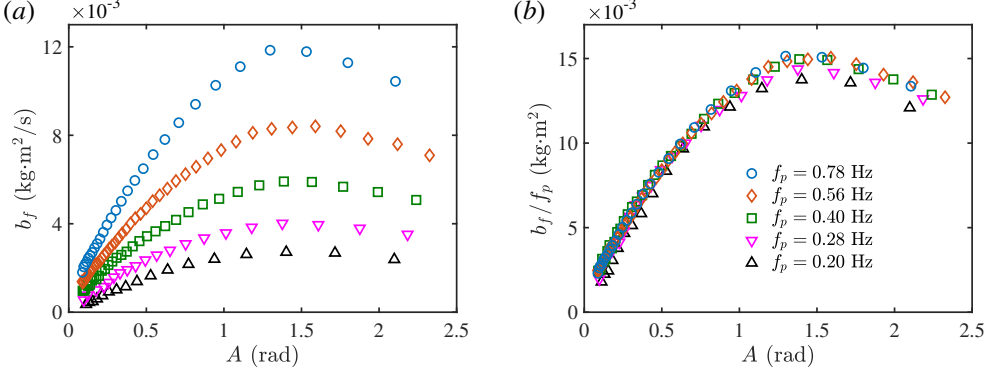


FIGURE 3. (a) Extracted fluid damping b_f at different pitching frequencies for $x/c = 0.5$. (b) A frequency scaling for the fluid damping which collapses b_f at different f_p into one curve. Note that (a) and (b) share the same legend.

3.2. Frequency scaling of the fluid damping

We repeat the ‘ring down’ experiment for the unswept wing ($\Lambda = 0^\circ$) pivoting at the mid-chord, $x/c = 0.5$, and change the pitching frequency by tuning the virtual inertia, I_v , and the virtual stiffness, k_v , while keeping the virtual damping b_v constant (Onoue & Breuer 2016, 2017). The extracted fluid damping, b_f , are shown in figure 3(a). Note that figure 3(a) and (b) share the same legend. We observe that b_f increases monotonically with the pitching frequency, f_p , and that the trend of b_f remains consistent for all frequencies. This observation agrees with those observed in heaving rigid plates (Keulegan & Carpenter 1958; Shih & Buchanan 1971), where the fluid damping coefficient scales inversely with the oscillation period. As we discussed earlier, b_f derives from the fluid damping torque τ_b , which depends strongly on the vortex-induced forces on the wing (Kang & Shyy 2014). Onoue & Breuer (2016, 2017) have shown that the circulation of LEVs scales with the strength of the feeding shear-layer velocity. In our case without a free-stream flow, the feeding shear-layer velocity equals the leading-/trailing-edge velocity, which is proportional to f_p . Based on this, we divide b_f by f_p (figure 3b). It is seen that with this scaling, all of the fluid damping curves collapse nicely.

We extend this frequency scaling to unswept wings with different pivot axes (figure 4a) and to swept wings with different sweep angles (figure 4b). For comparison, we include the previous results (figure 3b) using purple circles in both figure 4(a) and (b). Note that each symbol shape in figure 4 contains five different pitching frequencies, $f_p = 0.20, 0.28, 0.40, 0.56$ and 0.78 Hz.

For the unswept wing ($\Lambda = 0^\circ$), we change the pivot axis from $x/c = 0$ to 1 with a step size of 0.125 (see the inset of figure 4a). We observe that b_f/f_p increases as the pivot axis is moved away from the mid-chord, $x/c = 0.5$. For pivot axes that are symmetric with respect to the mid-chord (i.e. $x/c = 0.375$ & 0.625 , 0.25 & 0.75 , 0.125 & 0.875 and 0 & 1), b_f/f_p roughly overlap. The slight inconsistency between b_f/f_p for $x/c > 0.5$ and $x/c < 0.5$ comes from the asymmetry of the NACA 0012 wing geometry with respect to the mid-chord; we see that the scaled damping, b_f/f_p , is always slightly higher for $x/c < 0.5$. In these cases, the damping at the trailing edge dominates due to the higher velocity and longer moment arm, and is stronger than the cases when $x/c > 0.5$, where the leading-edge damping dominates. We will show in §3.4 that this is due to differences in the vortex structures generated by the sharp and rounded geometries.

This frequency scaling, b_f/f_p , also holds for three-dimensional (3D) swept wings (figure

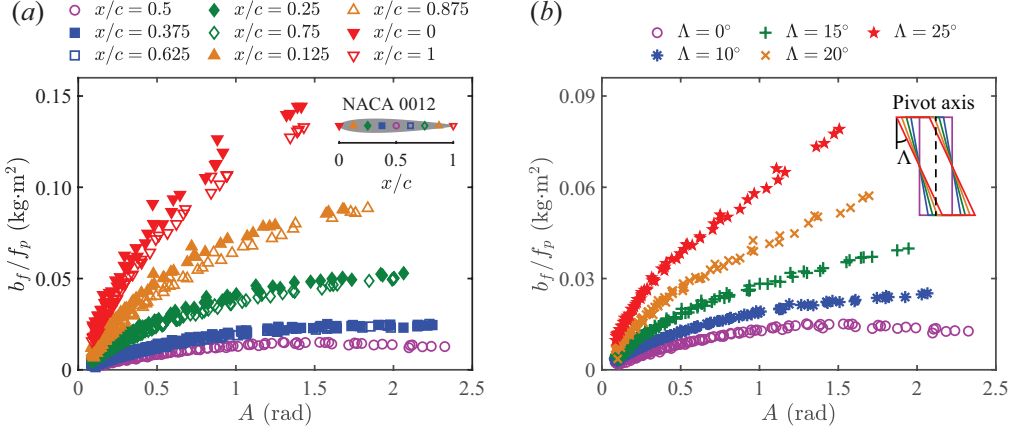


FIGURE 4. (a) b_f/f_p for an unswept wing ($\Lambda = 0^\circ$) pivoting at $x/c = 0$ to 1 with a step size of 0.125. The pivot location for each dataset is shown by the inset. (b) b_f/f_p for swept wings with $\Lambda = 0^\circ, 10^\circ, 15^\circ, 20^\circ$ and 25° . The inset shows side views of the five swept wings and the dashed line indicates the pivot axis. The colours of the wings correspond to the colours of b_f/f_p curves in the figure. The purple circles in (a) and (b) are replotted from figure 3(b). Note that each dataset in (a) and (b) includes five different f_p .

4b). Again, each curve includes data from five pitching frequencies. Here, the pivot axes of swept wings are kept as a vertical line passing through the mid-chord of the mid-span plane (see the inset of figure 4b). As Λ increases, the average pivot axes of the top and the bottom portion of the swept wing move away from the mid-chord, leading to the increase of the scaled damping, b_f/f_p , in a manner similar to that observed for unswept wings with different pivot locations (figure 4a). This argument will be revisited in the next section.

3.3. Universal fluid damping scaling for unswept and swept wings

Figure 4(a) indicates that the pivot axis plays an important role in determining the fluid damping of unswept wings. We extend the frequency scaling of b_f to take into account this effect. First, we divide the wing into two parts, the fore part from LE to the pivot axis with a chord length of c_{LE} , and the aft part from the pivot axis to TE with a chord length of c_{TE} (see the inset of figure 5 for an example when the wing pivots at $x/c = 0.5$). The Morison equation (Morison *et al.* 1950) indicates that the fluid damping force F scales with $0.5\rho U^2 sc$, where ρ is the fluid density, $U \sim \dot{\theta}c$ is the characteristic velocity and sc is the wing area. We can express the total fluid damping torque as the sum of the torque exerted on the fore and aft portions of the wing,

$$\tau_b \sim K_{LE} F_{LE} c_{LE} + K_{TE} F_{TE} c_{TE}, \quad (3.1)$$

where the subscripts LE and TE refer to the leading- and trailing-edge contributions, and K_{LE} and K_{TE} are empirical factors that account for the subtle differences in the damping associated with the specific geometries of the leading and trailing edges (figure 4a). Since the differences are small, K_{LE} and K_{TE} should be close to one, and for consistency, their average value must equal one ($(K_{LE} + K_{TE})/2 = 1$).

Since the damped oscillations are observed to be near-sinusoidal (figure 2a), the average angular velocity is given by $4f_p A$. Simplifying, we arrive at an expression for the fluid damping:

$$b_f \sim 2\rho f_p A s (K_{LE} c_{LE}^4 + K_{TE} c_{TE}^4), \quad (3.2)$$

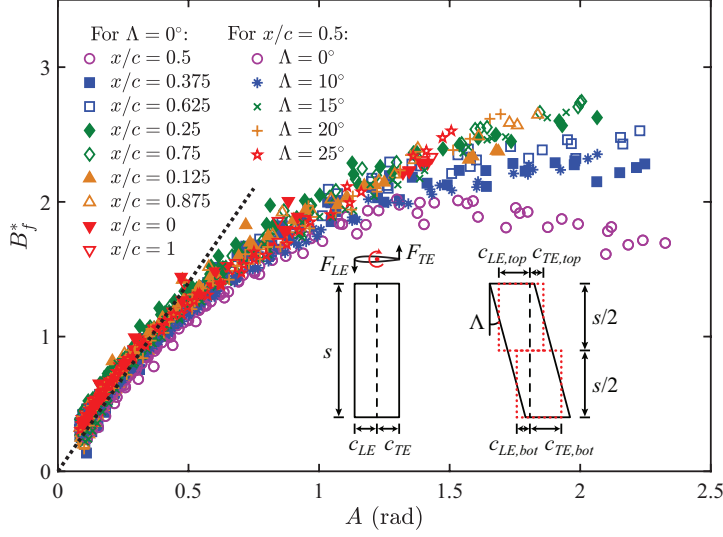


FIGURE 5. Non-dimensional fluid damping coefficient B_f^* versus pitching amplitude A for unswept wings pivoting at $x/c = 0$ to 1 and swept wings with sweep angles $\Lambda = 0^\circ$ to 25° . The inset shows the definition of the leading-edge chord c_{LE} and the trailing-edge chord c_{TE} , with black dashed lines indicating the pivot axes. The black dotted line indicates the small amplitude prediction for a drag coefficient of $C_D = 2.8$.

or, in non-dimensional form,

$$B_f^* \equiv \frac{b_f}{2\rho f_p s (K_{LE} c_{LE}^4 + K_{TE} c_{TE}^4)} \propto A. \quad (3.3)$$

For swept wings, because the pivot axis passes through $x/c = 0.5$ at the mid-span, the top half of the wing has an average pivot axis $x/c > 0.5$, while the bottom half has an average pivot axis $x/c < 0.5$. Ignoring three-dimensional effects, we approximate the swept wing by two ‘equivalent’ unswept wing segments. We choose not to divide the wing into a large number of narrow ‘blade elements’ (Glauert 1983), because the pivot axis of some elements near the wing root/tip for large sweep angles may lie outside the range $x/c = [0, 1]$, where our scaling has not been tested. The inset of figure 5 shows how these two unswept wing segments are configured (rectangles with red dotted lines). Based on the wing geometry, we see that

$$\begin{aligned} c_{LE,top} &= c_{TE,bot} = \frac{c}{2} + \frac{s}{4} \tan \Lambda, \\ c_{TE,top} &= c_{LE,bot} = \frac{c}{2} - \frac{s}{4} \tan \Lambda. \end{aligned} \quad (3.4)$$

Following the same analysis as for the unswept wing, and adding the fluid damping of the top and the bottom wing segments together, we find that the fluid damping for the full swept wing is given by

$$b_f \sim \rho f_p A s (K_{LE} c_{LE,top}^4 + K_{TE} c_{TE,top}^4 + K_{LE} c_{LE,bot}^4 + K_{TE} c_{TE,bot}^4). \quad (3.5)$$

If we define an effective leading-edge chord $c_{LE} = c_{LE,top} = c_{TE,bot}$ and an effective trailing-edge chord $c_{TE} = c_{TE,top} = c_{LE,bot}$, this scaling reduces to equation 3.2 with K_{LE} and K_{TE} cancelled out. This cancellation results because the effective pivot axes of the top and the bottom segments are symmetric about $x/c = 0.5$ at the mid-span, which averages out the slight differences in fluid damping experienced by the top and the bottom segments. For the same reason, K_{LE} and K_{TE} also cancel out in equation 3.3 for swept wings.

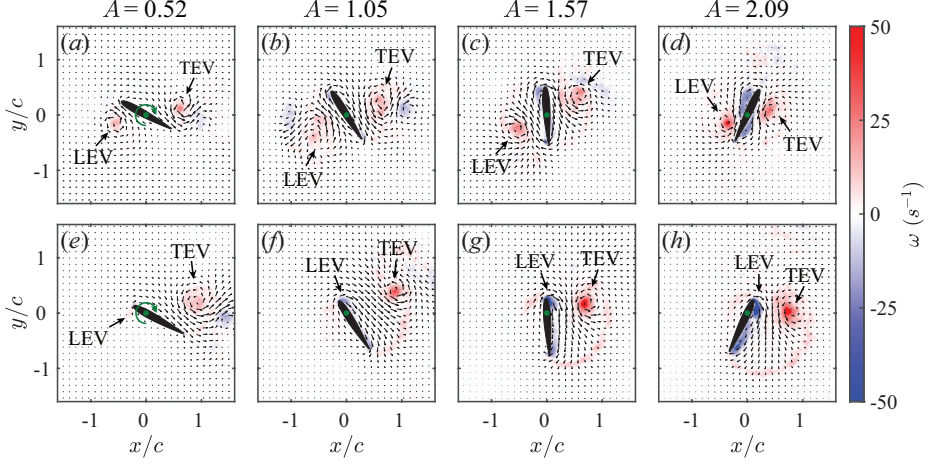


FIGURE 6. PIV flow field measurements for an unswept wing undergoing prescribed sinusoidal pitching motions in quiescent water. (a–d) Pivot axis (shown by green dots) $x/c = 0.5$, pitching frequency $f_p = 0.5$ Hz, pitching amplitude $A = 0.52$ (30°), 1.05 (60°), 1.57 (90°) and 2.09 (120°). (e–h) Same as (a–d), except that the pivot axis is at $x/c = 0.25$. All the velocity fields are phase-averaged over 20 cycles. Only every fifth velocity vector is shown. Spanwise vorticity ω : positive (red), counterclockwise; negative (blue), clockwise. See supplementary materials for the full video.

Figure 5 shows the non-dimensional fluid damping, B_f^* , as a function of the pitching amplitude, A , for unswept and swept wings. Here, we have used $K_{LE} = 0.95$ and $K_{TE} = 1.05$. We see that all of our measurements collapse remarkably well under the proposed scaling, especially for $A < 1.57$ (90°), despite the wide range of pitching frequencies ($f_p = 0.20$ to 0.78 Hz), pivot axes ($x/c = 0$ to 1) and sweep angles ($\Lambda = 0^\circ$ to 25°) tested in the experiments. In the small-amplitude limit ($A < 0.5$), B_f^* scales linearly with A , with a slope that corresponds to the drag coefficient, C_D . We note that $C_D \approx 2.8$, which is comparable to that of an accelerated normal flat plate (Ringuette *et al.* 2007). At higher pitching angles ($A > 0.5$), however, the linear approximation no longer holds and we see a decreasing slope of B_f^* as a function of A . This is presumably because the shed vortices no longer follow the rotating wing and the fluid force becomes non-perpendicular to the wing surface as A increases. For $A > 1.57$ (90°), the scaling works reasonably well except for the case $\Lambda = 0^\circ$, $x/c = 0.5$, where a decreasing B_f^* is observed. In the next section, we will use insights from the velocity fields to explain this non-monotonic behaviour.

3.4. Insights obtained from velocity fields

To gain more insight regarding the nonlinear behaviour of B_f^* , we conduct 2D PIV experiments to measure the surrounding flow fields of an unswept wing ($\Lambda = 0^\circ$) with a prescribed pitching motion: $\theta = A \sin(2\pi f_p t)$. The results are shown in figure 6. The pitching frequency is kept at $f_p = 0.5$ Hz for all the cases and the pitching amplitude is varied from $A = 0.52$ (30°) to 2.09 (120°) with a step size of 0.52 (30°). Two pivot axes are tested, $x/c = 0.5$ (figure 6a–d) and $x/c = 0.25$ (figure 6e–h). Note that the flow fields shown in figure 6 are *not* sequential. Instead, all the snapshots are taken right before $t/T = 0.25$ for different pitching amplitudes, where T is the pitching period. This specific time instant is chosen because it best reflects the difference in dynamics associated with the different pitching amplitudes and pivot axes.

For both pivot locations (figure 6a–d: $x/c = 0.5$ and e–h: $x/c = 0.25$), the spanwise vorticity of the pitch-generated leading-edge vortex (LEV) and trailing-edge vortex (TEV)

increases with the pitching amplitude, A . This can be explained by the increase in the feeding shear-layer velocities associated with the higher pitching amplitudes (Onoue & Breuer 2016). The boundary vortices near the wing surface, which are related to the added mass effect (Corkery *et al.* 2019), also become more prominent due to the increase of the angular acceleration. When the wing pivots at $x/c = 0.5$ (figure 6*a–d*), the leading-edge velocity equals the trailing-edge velocity. As a result, the LEV and TEV are fairly symmetric about the pivot axis, with some subtle differences caused by the rounded and sharp edges, respectively. This confirms the arguments given earlier for the differences between b_f/f_p for $x/c > 0.5$ and $x/c < 0.5$ (figure 4*a*). For $x/c = 0.25$ (figure 6*e–h*), however, the TEV is much more prominent than the LEV because of the higher trailing-edge velocity. Due to the low leading-edge velocity and the pitch-induced rotational flow, the sign of the LEV even reverses and becomes negative for $A = 1.05$ to 2.09 (figure 6*f–h*).

For both pivot locations, due to the absence of a convective free stream, and the existence of the pitch-induced rotational flow, the LEV and TEV (only the TEV for $x/c = 0.25$) are entrained closer to the wing surface as A increases. For $x/c = 0.5$, as shown in figure 6(*c–d*), the LEV moves towards the aft portion of the wing and the TEV moves towards the fore portion of the wing when $A \geq 1.57$ (90°). The torque generated by these two vortices, which counteracts the wing rotation for small A , now assists the rotation as the wing pitches up towards higher angular positions. This assist reduces the fluid drag experienced by the wing and thus lowers the fluid damping. This effect can account for the non-monotonic behaviour of B_f^* for $x/c = 0.5$ (figure 5). For $x/c = 0.25$ (figure 6*g–h*), a similar scenario is observed, in which the TEV moves towards the fore portion of the wing and gets closer to the wing surface as A increases. However, because of the existence of a counter-rotating LEV, the TEV is not able to approach the wing surface as closely as in the $x/c = 0.5$ case. This explains why a flattening behaviour, rather than a non-monotonic trend of B_f^* , is observed for $x/c = 0.25$ and presumably for other pivot locations at high pitching amplitudes.

4. Conclusions

By utilising a cyber-physical control system to create an elastically mounted pitching wing, we have experimentally measured the nonlinear fluid damping associated with vortices shed from a bluff body. A theoretical scaling has been proposed and validated, based on the Morison equation, which incorporates the frequency, amplitude, pivot location and sweep angle. The nonlinear behaviour of the scaled fluid damping has been correlated with the velocity fields measured using particle image velocimetry.

One should note that our scaling may not be applicable for instantaneous fluid damping, because the damping characterised in the present study is cycle-averaged over near-sinusoidal oscillations. In addition, we have not considered three-dimensional effects, which are present due to the wing tip flows. Incorporating these may further improve the collapse of the fluid damping coefficient, B_f^* (figure 5). Lastly, in §3.4, only qualitative analysis of the flow field has been performed thus far. In order to get more accurate correspondence between the fluid damping and the flow dynamics, quantitative analysis of the vortex trajectory and circulation is needed, which will be the focus of future study.

Despite these limitations, the proposed scaling has been shown to collapse the data over a wide range of operating conditions ($f_p = 0.20$ to 0.78 Hz and $A = 0$ to 2.5) for both unswept ($x/c = 0$ to 1) and swept wings ($\Lambda = 0^\circ$ to 25°). It can be used to predict damping associated with shed vortices, and thus benefit the future modelling of a wide variety of flows, including unswept and swept wings in unsteady flows as well as other bluff body geometries. The universality of this scaling reinforces the underlying connection between swept wings and

unswept wings with different pivot locations. In addition, the results presented in this study will be of potential value as a source of experimental data for validation and comparison of future theoretical/computational models.

Acknowledgments

This work is funded by Air Force Office of Scientific Research, Grant FA9550-18-1-0322, managed by Dr. Gregg Abate.

REFERENCES

- ALBEN, S. 2008 Optimal flexibility of a flapping appendage in an inviscid fluid. *J. Fluid Mech.* **614**, 355.
- BEATUS, T. & COHEN, I. 2015 Wing-pitch modulation in maneuvering fruit flies is explained by an interplay between aerodynamics and a torsional spring. *Phys. Rev. E* **92** (2), 022712.
- BERGOU, A. J., XU, S. & WANG, Z. J. 2007 Passive wing pitch reversal in insect flight. *J. Fluid Mech.* **591**, 321–337.
- BRENNEN, C. E. 1982 A review of added mass and fluid inertial forces. *Tech. Rep.*. Naval Civil Engineering Laboratory.
- CORKE, T. C. & THOMAS, F. O. 2015 Dynamic stall in pitching airfoils: aerodynamic damping and compressibility effects. *Annu. Rev. Fluid Mech.* **47**, 479–505.
- CORKERY, S. J., BABINSKY, H. & GRAHAM, W. R. 2019 Quantification of added-mass effects using particle image velocimetry data for a translating and rotating flat plate. *J. Fluid Mech.* **870**, 492–518.
- DOWELL, E. H., CURTISS, H. C., SCANLAN, R. H. & SISTO, F. 1989 *A modern course in aeroelasticity*. Springer.
- DUGUNDJI, J. 2008 Some aeroelastic and nonlinear vibration problems encountered on the journey to ithaca. *AIAA J.* **46** (1), 21–35.
- GLAUERT, H. 1983 *The elements of aerofoil and airscrew theory*. Cambridge University Press.
- KANG, C.-K. & SHYY, W. 2014 Analytical model for instantaneous lift and shape deformation of an insect-scale flapping wing in hover. *J. R. Soc. Interface* **11** (101), 20140933.
- KEULEGAN, G. H. & CARPENTER, L. H. 1958 Forces on cylinders and plates in an oscillating fluid. *J. Res. Natl. Bur. Stand.* **60** (5), 423–440.
- MATHAI, V., LOEFFEN, L. A. W. M., CHAN, T. T. K. & WILDEMAN, S. 2019 Dynamics of heavy and buoyant underwater pendulums. *J. Fluid Mech.* **862**, 348–363.
- MCCROSKEY, W. J. 1982 Unsteady airfoils. *Annu. Rev. Fluid Mech.* **14** (1), 285–311.
- MENON, K. & MITTAL, R. 2019 Flow physics and dynamics of flow-induced pitch oscillations of an airfoil. *J. Fluid Mech.* **877**, 582–613.
- MORISON, J. R., JOHNSON, J. W. & SCHAAF, S. A. 1950 The force exerted by surface waves on piles. *J. Pet. Technol.* **2** (05), 149–154.
- ONOE, K. & BREUER, K. S. 2016 Vortex formation and shedding from a cyber-physical pitching plate. *J. Fluid Mech.* **793**, 229–247.
- ONOE, K. & BREUER, K. S. 2017 A scaling for vortex formation on swept and unswept pitching wings. *J. Fluid Mech.* **832**, 697–720.
- RAO, S. S. 1995 *Mechanical Vibrations*. Addison-Wesley.
- RINGUETTE, M. J., MILANO, M. & GHARIB, M. 2007 Role of the tip vortex in the force generation of low-aspect-ratio normal flat plates. *J. Fluid Mech.* **581**, 453–468.
- SHIH, C. C. & BUCHANAN, H. J. 1971 The drag on oscillating flat plates in liquids at low reynolds numbers. *J. Fluid Mech.* **48** (2), 229–239.
- SHINDE, S. Y. & ARAKERI, J. H. 2013 Jet meandering by a foil pitching in quiescent fluid. *Phys. Fluids* **25** (4), 041701.
- SU, Y. & BREUER, K. S. 2019 Resonant response and optimal energy harvesting of an elastically mounted pitching and heaving hydrofoil. *Phys. Rev. Fluids* **4** (6), 064701.
- TZEZANA, G. A. & BREUER, K. S. 2019 Thrust, drag and wake structure in flapping compliant membrane wings. *J. Fluid Mech.* **862**, 871–888.
- WANG, Z. J. 2005 Dissecting insect flight. *Annu. Rev. Fluid Mech.* **37**, 183–210.

- XIAO, Q. & ZHU, Q. 2014 A review on flow energy harvesters based on flapping foils. *J. Fluids Struct.* **46**, 174–191.
- YOUNG, J., LAI, J. C. S. & PLATZER, M. F. 2014 A review of progress and challenges in flapping foil power generation. *Prog. Aerosp. Sci.* **67**, 2–28.
- ZHU, Y., SU, Y. & BREUER, K. S. 2020 Nonlinear flow-induced instability of an elastically mounted pitching wing. *J. Fluid Mech.* **899**, A35.